THE JOURNAL OF PHYSICAL CHEMISTRY C

Article

pubs.acs.org/JPCC

Role of Surface Plasmons and Hot Electrons on the Multi-Step Photocatalytic Decay by Defect Enriched Ag@TiO_2 Nanorods under Visible Light

Kamal Kumar Paul[†] and P. K. Giri*[,†,‡]

[†]Department of Physics, and [‡]Centre for Nanotechnology, Indian Institute of Technology Guwahati, Guwahati 781039, India

S Supporting Information

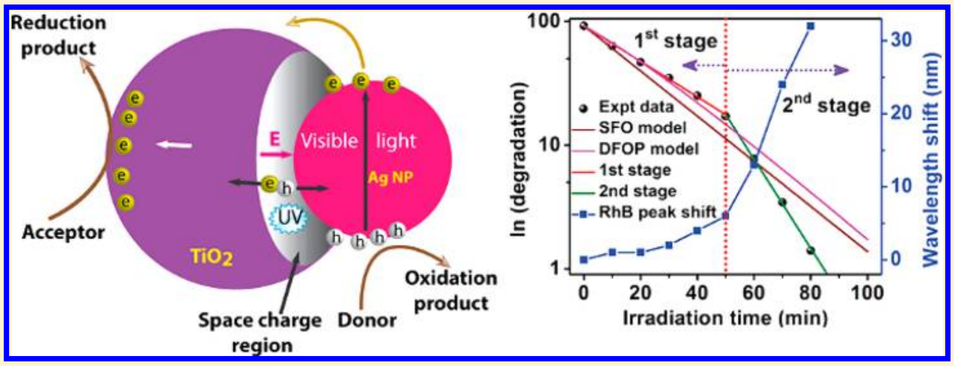

ABSTRACT: Heterogeneous photocatalysis is of overriding significance for emerging energy and environment applications. Nanosized metal−semiconductor heterostructures (HSs) allow extraordinarily tuned and intense absorption of light, making it very promising for efficient solar energy harvesting in photovoltaic and photocatalytic applications. Here we report on the ultrahigh rate of photodegradation of organic dye, Rhodamine-B, with two distinct sequential degradation rate processes under visible light illumination on Ag nanoparticle (NP) decorated anatase TiO_2 nanorods (NRs) grown by a solvothermal route. HRTEM analysis reveals the uniform decoration of Ag NPs (∼17 nm) over the TiO_2 NRs surface for the optimized Ag@TiO_2 HS. The defect rich Ag@TiO_2 NR HSs grown with an optimal weight ratio Ag:TiO_2 = 3:2 (TA32) exhibit very strong optical absorption due to the localized surface plasmon resonance (LSPR) effect over the entire visible region, having an absorption peak at ∼520 nm. The effective band gap of TA32 has been significantly reduced to 2.71 eV from the pure TiO_2 band gap of 3.2 eV. Studies on photocatalysis of Rhodamine-B show a very high degradation rate for the HSs due to the LSPR effect in the noble Ag NPs and fast charge transfer at the Ag@TiO_2 interface. The optimized heterostructure (TA32) exhibits nearly double plasmonic absorbance than the other HSs, and it shows the highest degradation rate under visible light irradiation. In contrast to the available models, in the present case the degradation kinetics follows a sequential rate process with two distinct exponential decay functions/rate constants. For the optimized HS (TA32), the degradation rate constants are found to be 0.083 (k_2) and 0.033 min^{-1} (k_1) in the second and first stages of degradation, respectively. The pseudo first order rate constant was >4 times higher in the first stage and ∼10 times stronger in the second stage of degradation for TA32 HS in comparison to the bare TiO_2 NRs as well as commercial P25. Our results demonstrate the long-term stability and superiority of the Ag@TiO_2 HS over the bare TiO_2 NRs and other TiO_2 based photocatalysts for detoxification of air/water. This study offers new insights in understanding the mechanism of advanced photocatalysis with multi rate constants by oxygen vacancy enriched Ag@TiO_2 nanoheterostructures.

1. INTRODUCTION

Photocatalysis is believed to be one of the most promising technologies to solve the problems associated with environmental pollution and ever increasing energy crises.[1−3] Due to strong oxidizing capacity, nontoxicity, environmental friendliness, abundant availability, and good degradation efficiency, TiO_2 is regarded as the most favorable material for wastewater remediation, water splitting, and solar cell applications.[4−7] However, TiO_2 as a typical semiconductor has a band gap of ∼3.2 eV, and thus the activation of its photocatalytic activity requires UV light that contributes to less than 5% of the sunlight; thus, band gap tuning is necessary to make TiO_2 active under the broader band of the solar spectrum.[8,9] In addition, a high recombination rate and low efficiency of separating the photogenerated electron−hole pairs to the surface of the semiconductor photocatalysts limit its industry related practical application. To overcome these difficulties, various approaches are being explored to achieve solar light activation; especially in the visible and NIR region, including doping with nonmetal elements,[10−12] surface sensitization with

Received: June 1, 2017
Revised: August 1, 2017
Published: August 18, 2017

organic dyes,[13] defect incorporation,[14−18] coupling with narrow band gap semiconductors,[8,19−21] modifying morphology, and exploring the localized surface plasmon resonance (LSPR) by plasmonic nanoparticles (NPs), e.g., Ag, Au, Pd, Pt,[22−24] etc. A properly designed plasmonic nanostructure can drive coherent oscillation of confined free electrons on metal NPs with the identical frequency as the incident radiation known as LSPR, which in turn creates an intense, highly localized electromagnetic field.[25] After the light absorption and LSPR excitation in the plasmonic nanostructures, a nonradiative decay of energy takes place on a femtosecond time scale by transferring the energy to the nearest hot electrons.[26] LSPR is reported to play an important role in the enhancement of the photocatalytic performance under visible light irradiation. Among various plasmonic materials, Ag has been shown to be the most significant, and thus Ag based various nanostructures, like Ag@AgCl,[27] Ag/AgCl/TiO_2,[28] Ag/TiO_2,[29] and Ag_2O/TiO_2,[8] have been studied extensively. However, most of these studies have focused on the UV light photocatalysis process. Further, the hot electrons having an energy (1−4 eV)[26] greater than the Schottky barrier between a plasmonic nanostructure and semiconductor can easily migrate from the metal to semiconductor surface, and the internal electric field developed at the space charge region and inside the defective n-type TiO_2 accelerates this charge separation at the metal/semiconductor interface.[30] Thus, plasmonic nanostructures possess highly enhanced photocatalytic activity under visible light irradiation by lowering the activation energy.

Despite intense research on the TiO_2 based plasmonic nanostructures for photocatalysis, a proper understanding of the mechanism of catalytic enhancement and the degradation rate kinetics of the material is still lacking. To our knowledge, the Ag@TiO_2 heterostructure (HS) with two distinct degradation rate constants has not been explored yet for the visible light photocatalysis of organic dyes.

Though several studies have focused on plasmonic Ag NP decorated TiO_2 nanostructures, insights into the mechanism and the rate kinetics of photocatalytic degradation are still not fully understood. Cheng et al.[31] studied the degradation of RhB with Ag@TiO_2 core−shell nanostructure and obtained almost full decomposition but with the UV light irradiation. Additionally, Chen et al.,[32] Wang et al.,[33] and Cui et al.[34] have studied the photocatalytic dye degradation by Ag, Ag_2O, and AgBr incorporated TiO_2 nanostructures assuming pseudo first order rate kinetics with single rate constant. However, the presented data does not fit well with the first order rate kinetics.

Here, we have grown Ag NP decorated TiO_2 NRs by a modified solvothermal method followed by a photoreduction method. The surface decoration of TiO_2 NRs with Ag NPs was confirmed from the HRTEM, EDX, and XPS analyses. Ag@TiO_2 HSs are shown to have superior photocatalytic performance as compared to the bare TiO_2 NRs owing to their extremely high visible light absorption and tuned effective band gap. Visible light photocatalytic activity of the Ag@TiO_2 composite has been investigated using aqueous Rhodamine-B (RhB) as the reference dye. We report on the sequential process of degradation kinetics and thus two separate degradation rate constants by defect enriched Ag@TiO_2 HSs. We have found a massive enhancement (∼10 times) in the degradation rate constant for an optimized HS sample as compared to the bare TiO_2 NRs as well as commercial P25 photocatalyst.

2. EXPERIMENTAL PROCEDURES

2.1. Preparation of TiO_2 NRs. TiO_2 NRs were synthesized by a typical solvothermal process in concentrated NaOH solution with DI water and ethylene glycol in a 1:1 volume ratio. In a typical synthesis, 1 g of precursor anatase TiO_2 powder (Merck, average particle size ∼80 nm) was mixed with 48 mL of 10 M NaOH mixed solvent (DI water:ethylene glycol = 1:1) under stirring for 1 h, followed by hydrothermal treatment in a 100 mL Teflon-lined autoclave (Berghof, BR-100). The temperature inside the autoclave chamber was measured and maintained at 180 °C under autogenous pressure and constant magnetic stirring at 500 rpm for 16 h. The formed precipitates were washed thoroughly with DI water and obtained by centrifugation followed by a drying process at 80 °C. The obtained sodium titanate NRs were treated ultrasonically with 0.1 N HCl until the pH reduces nearly to 7, which ensures the total exchange of sodium ions with protons. Then the precipitates were washed several times with DI water to obtain hydrogen titanate NRs, and subsequently, the H-titanate NRs were calcined at 700 °C for 5 h in air to grow pure anatase TiO_2 NRs.

2.2. Growth of Ag@TiO_2 NRs HSs. Ag@TiO_2 NR HSs with various weight ratios (Ag:TiO_2) from 1:2 to 2:1 were synthesized by a photoreduction method. Typically for a 1:1 weight ratio, 0.05 g of TiO_2 NRs was dispersed in 25 mL of ethanol, and then 0.42 g of $AgNO_3$ (0.1 M) was dissolved into the above suspended solution. The above mixture was then stirred magnetically for 1 h to reach adsorption equilibrium. Subsequently, the suspension was irradiated by a 250 W UV lamp for 5 min under vigorous magnetic stirring to form the Ag NPs on the TiO_2 platform. The Ag@TiO_2 HS was obtained by washing it with DI water several times, filtration, and drying process. A summary of the samples studied with sample codes is presented in Table 1.

Table 1. Sample Specification and Effective Band Gap of Different Samples, Calculated from the Respective Tauc Plot

sample composition			
weight ratio of			
Ag	TiO_2	sample code	effective band gap (eV)
0	1	TiO_2	3.20
1	1	TA11	2.89
1	2	TA12	3.00
2	1	TA21	2.94
2	3	TA23	3.03
3	2	TA32	2.71

2.3. Characterization Techniques. The crystal structure of the as-grown catalysts has been confirmed from X-ray powder diffraction (XRD) pattern (Rigaku RINT 2500 TTRAX-III, Cu Kα radiation). The crystallinity and phase composition of the as-synthesized NRs have been measured by micro-Raman spectroscopy (LabRam HR800, Jobin Yvon). The morphology, size, and the elemental compositions of the as-synthesized TiO_2 NRs and Ag@TiO_2 HSs have been studied by a field emission scanning electron microscope (FESEM; Sigma, Zeiss) equipped with an energy dispersive X-ray (EDX) spectrometer. The high magnification surface morphologies and structures of the as-grown samples have been studied by a transmission electron microscope (TEM; JEOL-JEM 2010 operated at 200 kV). Samples for TEM analysis have been

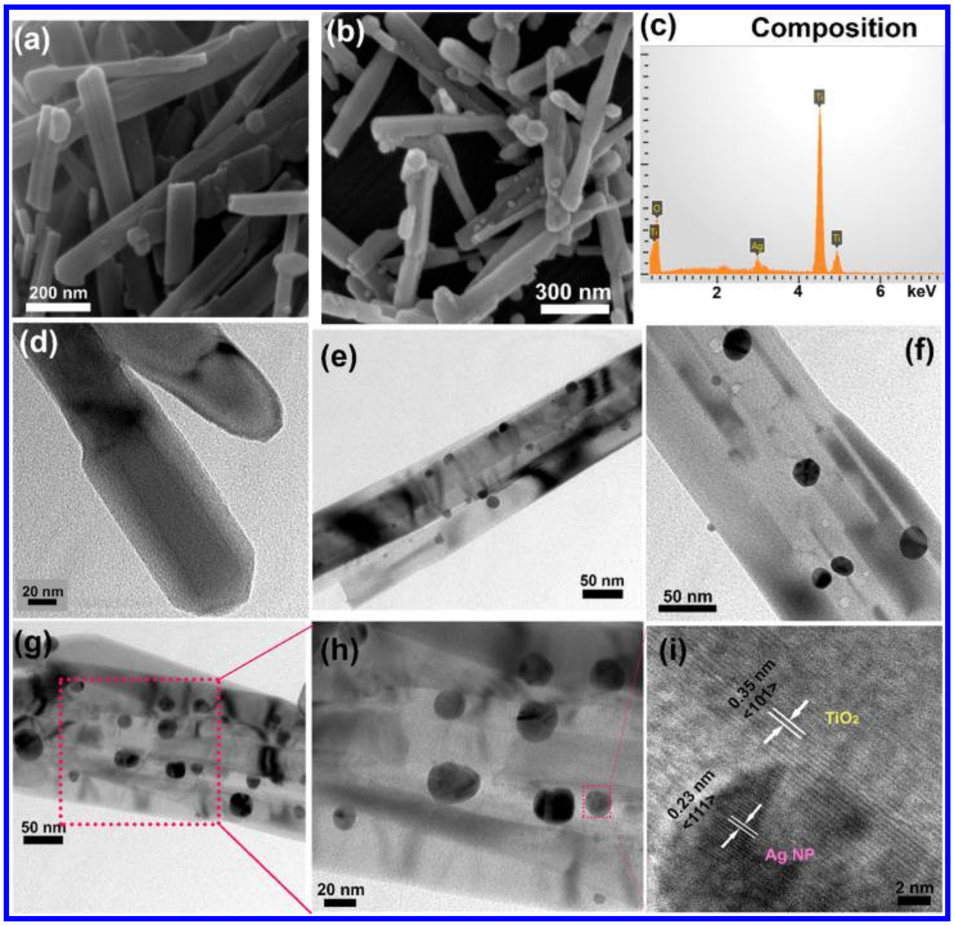

Figure 1. FESEM images of TiO_2 NRs: (a) before, (b) after Ag decoration, and (c) the EDX spectrum of TiO_2 NRs after Ag decoration. (d) TEM image of faceted TiO_2 NRs and (e and f) TEM images of TA12 and TA21 HS, respectively. (g) TEM image of TA32 HS showing Ag NP decoration, (h) the enlarged view of image in panel g, and (i) HRTEM lattice image of HS showing the lattice spacing of Ag and TiO_2 with respective crystal orientations.

prepared on a carbon coated Cu grid of 400 mesh size (Pacific Grid, U.S.A.). UV−visible absorption spectra were measured from diffuse reflectance spectroscopy (DRS) measurements of the samples using a commercial spectrophotometer (PerkinElmer, UV win Lab). X-ray photoelectron spectroscopy (XPS) has been carried out using a PHI X-tool automated photoelectron spectrometer (ULVAC-PHI, Japan) with an Al Kα X-ray beam (1486.6 eV) at a beam current of 20 mA. The shift in the binding energy of various elements has been corrected using the C 1s spectrum at 284.8 eV as a standard value.[8] The room temperature steady state photoluminescence (PL) spectra have been recorded by using a 355 nm diode laser excitation with the help of a single grating monochromator (Triax 550) and a cooled CCD detector (Jovin Yvon). Time resolved photoluminescence (TRPL) spectra have been recorded in a picosecond time-resolved fluorescence spectrometer (Edinburg Instruments, FSP920). Photoconductivity measurement was performed on the bare TiO_2 and TA32 HS samples in the form of pellets (diameter 10 mm) using a xenon lamp source and a microprobe station (ECOPIA EPS-500) connected to a source meter (Keithley 2400) to measure the dark-current and photocurrent under a constant bias voltage. A 300 W xenon lamp (Oriel Instruments, U.S.A.) equipped with a 400 nm cutoff filter was used as a light source to excite the sample. This ensures that the sample is excited only with the visible light. The setup is interfaced with a computer to collect the data using Lab Tracer 2.0 software. Photocatalytic activity of the synthesized photocatalysts has been studied using a time programmable commercial photochemical reactor (Lelesil Innovative Systems, Mumbai) equipped with a visible lamp source (250 W).

2.4. Photocatalytic Degradation under Visible Light.

The photocatalytic activity of pure TiO_2 NRs and Ag@TiO_2 HSs has been evaluated considering the photodegradation of RhB as a model dye under visible light irradiation. In a typical experiment, 50 mL of an aqueous suspension of RhB (10 mg/L) and 20 mg of catalyst powders have been placed in a 100 mL beaker. Before visible light irradiation, the mixture of dye solution and photocatalyst were magnetically stirred under dark for 45 min. This allowed the establishment of adsorption−desorption equilibrium between the interface of the photocatalysts and dye molecules under ambient conditions. A 250 W lamp having emission in the range 390−800 nm was used as the light source for visible light photocatalysis. The lamp is surrounded by a water-cooled quartz jacket that absorbs the heat generated from the high power lamp. This maintains a constant temperature of the whole environment, and it ensures that the degradation occurred only because of light irradiation instead of heat. At chosen irradiation intervals, 3 mL of solution was collected and centrifuged to remove the catalyst particles from the dye for further study. In order to estimate the residual concentration of the dye solution, UV−vis absorbance was measured in a Shimadzu 2450 UV−vis spectrophotometer.

3. RESULTS AND DISCUSSION

3.1. Morphology Studies. The growth of TiO_2 NRs by the solvothermal process and the decoration of Ag NPs on the NRs by the photoreduction method have been discussed by several groups.[23,35] The typical morphology and microstructural properties of TiO_2 NRs and Ag@TiO_2 HSs were characterized by FESEM. Figure 1a shows the FESEM image of pure TiO_2 NRs with diameter ∼40−120 nm and lengths up to a few μm, while Figure 1b shows the FESEM image of Ag@TiO_2 HS (named as TA32, see Table 1). Though the Ag NPs decorated on TiO_2 NRs have sufficiently broad size distribution, particles only with size ≥30 nm were discernible due to the limitation of FESEM imaging. EDX analysis on the as-grown Ag@TiO_2 NR HSs reveals that it contains Ti, Ag, and O elements (shown in Figure 1c), as expected.

To study the high resolution surface morphology and structure of the NRs and their HSs, TEM images are acquired for the respective samples. Figure 1d shows the TEM image of a TiO_2 NR, while Figure 1e−g depicts the typical TEM images of Ag@TiO_2 for TA12, TA21, and TA32, respectively. Clearly Ag NPs are uniformly decorated over the TiO_2 NRs for all of the HS samples. Interestingly, the distribution of Ag NPs is highly uniform in the TA32 sample in comparison to the other HS samples. Figure 1h shows a closer view of Figure 1g, which further confirms that there not only exists a spatial uniformity of NPs but also is uniformity in size of Ag NPs. For a higher weight ratio of Ag/TiO_2, i.e., for TA21 (see Figure 1f), the distribution is still uniform but with some agglomeration, which may be due to the higher concentration of Ag. Figure 1e shows the TEM image of TA12, which reveals the uniform decoration of Ag NPs with nearly uniform size. In both of the cases of extremely high (TA21) and low (TA12) concentration of Ag, we observe a comparatively lower density of Ag NPs on TiO_2 surface, which may be due to the aggregation in the case of TA21 and lower concentration of precursor material for TA12. Figure 1i shows the HRTEM lattice image of TA32 HS, which clearly reveals the simultaneous presence of crystalline Ag and TiO_2. It is clear from Figure 1h,i that Ag NPs are decorated on the uneven TiO_2 surface, which enable a close contact between the two. Thus, the Ag NPs are coupled enough with the TiO_2 surface so that an efficient charge transport can be expected at the interface of the HS. Lattice spacing of TiO_2 and Ag has been calculated by measuring the intermediate distance between the lattice fringes. Pure anatase TiO_2 with (101) crystal planes (d = 0.35 nm) and cubic Ag with (111) crystal planes (d = 0.23 nm) are confirmed from the lattice fringe image. We have also plotted the size distribution and the log-normal fitting of Ag NPs on TiO_2 NRs for TA32 and TA21 in Figure S1 (Supporting Information). It is observed that the average size and broadening of distribution of decorated Ag NPs are increasing with increasing the Ag weight ratio. The average NP size and width of distribution were calculated as 17.64 and 0.27 nm for TA32 and 21.42 and 0.28 nm for TA21 respectively (see Figure S1). A higher concentration of $AgNO_3$ may be leading to the fusion of Ag NPs into larger size ones.

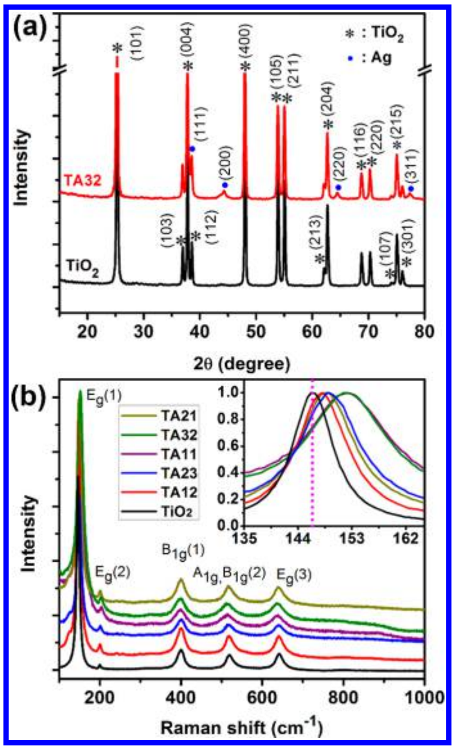

Figure 2. (a) XRD patterns of TiO_2 NRs and Ag@TiO_2 NR HS (TA32). The curves are vertically shifted for clarity of presentation. (b) Raman spectra of pristine TiO_2 NRs and Ag@TiO_2 NR HSs. The curves are vertically shifted for clarity of presentation. All Raman peaks correspond to the anatase phase of TiO_2. The inset shows a magnified view of the $E_g(1)$ peak for all samples. The dotted vertical line indicates the peak position of bare TiO_2 NRs, and it shows a clear shift of the $E_g(1)$ mode after Ag NPs loading.

3.2. Structural Analysis. *3.2.1. XRD Analysis.* In order to confirm the structure, phase, and crystallinity of the as-synthesized TiO_2 NRs and Ag@TiO_2 HSs, the XRD pattern of each sample has been recorded, and the results are shown in Figure 2a. Each diffraction peak of TiO_2 NRs (labeled with a star symbol) corresponds to pure anatase phase (JCPDS file no. 841285) and the peaks marked with blue circles (filled) imply the presence of Ag NPs, which matches exactly with the JCPDS file no. 040783. The diffraction peaks of TiO_2 are extremely sharp clearly implying its highly crystalline nature. The phases of anatase TiO_2 and Ag coexist in the Ag@TiO_2 HS crystals. Note that the XRD pattern of the HS sample shows a slight downshift in the TiO_2 peaks as compared to the pristine TiO_2 NRs. This may imply a tensile strain in the TiO_2 NRs in the HS due to strong coupling of the TiO_2 and Ag lattice, which is fully consistent with the Raman and XPS results discussed below.

3.2.2. Raman Analysis. Figure 2b shows a comparison of the micro-Raman spectra for all samples. The micro-Raman spectra of the anatase TiO_2 phase have six active Raman modes: $E_g(1)$, $E_g(2)$, $B_{1g}(1)$, A_{1g}, $B_{1g}(2)$, and $E_g(3)$, and the most prominent Raman mode, $E_g(1)$, appears at 144 cm^{-1}.[36] However, in the present case, the as-synthesized TiO_2 NRs show the $E_g(1)$ peak at 146.4 cm^{-1}, which may be due to the change in the oxygen stoichiometry in the TiO_2 crystal, as confirmed from the XPS analysis later. With the loading of Ag NPs, the Raman peaks become broadened and shift toward the higher frequency side, as detailed in Table-3. In particular, the blue shift and full width at half-maximum (fwhm) of the Raman peak is highest for the TA11 and TA32. Comparison of the Raman shift and fwhm of band $E_g(1)$ is shown as an inset in Figure 2b. As compared to bare TiO_2, the TA11 and TA32 samples show nearly double fwhm with blue shifts of ∼5.51 and ∼5.58 cm^{-1}, respectively. Such a high blue shift and the higher fwhm of $E_g(1)$ can be interpreted as nonstoichiometry in the TiO_2 lattice due to

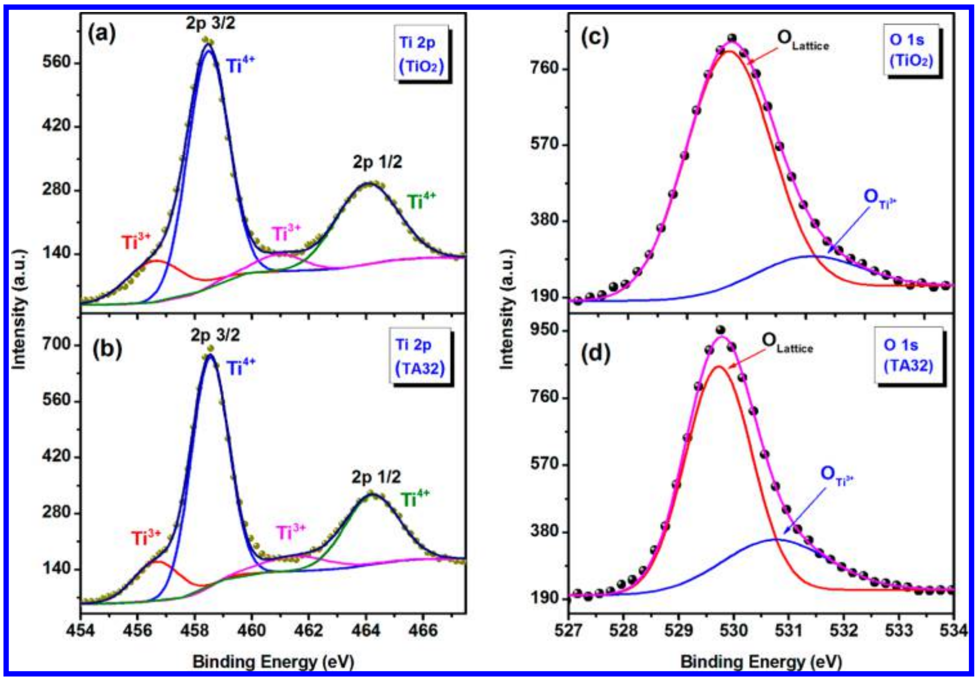

Figure 3. (a and b) Ti 2p core level XPS spectra for TiO_2 NRs and TA32 HS, respectively, fitted with Shirley baseline. The symbols represent the experimental data, and the solid lines correspond to the Gaussian fits. (c and d) The O 1s core level XPS spectra for TiO_2 and TA32 HS, respectively. The identity of each fitted peak is denoted with corresponding charge states in the respective cases.

oxygen vacancies, strain induced by the vacancy related Ti relaxation, and strong interaction between TiO_2 and Ag atoms.[37] It is understood that the oxygen vacancy/defects is increasing with the Ag loading amount and reaches an optimum value for the TA32 sample and then again it decreases. This may be due to the higher aggregation which leads to the formation of larger Ag NPs and consequently the interfacial contact and hence their interaction reduces. As the defects and disorders present in the TiO_2 lattice disturb the B_{1g} mode more intensely than the $E_g(1)$ mode,[35] we have studied the $B_{1g}(1)$ for all samples. A large broadening of the $B_{1g}(1)$ mode for the TA32 (fwhm = 35.22 cm^{-1}) and TA11 (34.00 cm^{-1}) samples has been observed as compared to that of the bare TiO_2 (20.44 cm^{-1}). Thus, Raman studies revealed that the blue-shift and increase in fwhm in the specific Raman band are due to the nonstoichiometric oxygen defects in the Ag@TiO_2 HSs.

3.2.3. XPS Analysis. To investigate the elemental composition, chemical valence state and surface defects of the TiO_2 nanostructures, XPS studies were carried out. Figure 3a,b shows the Ti 2p core level spectra of TiO_2 NRs and Ag@TiO_2 HS (TA32). Each peak has been deconvoluted with two symmetric Gaussian peaks. Surface defects present in TiO_2 NRs and the HS sample (TA32) were confirmed from the Ti 2p spectra. The major Ti 2p doublet peaks for both TiO_2 and TA32 HS exhibit a tail in the lower binding energy side, which indicates the presence of lower valence states of Ti (see Figure 3a,b). The main two peaks centered at around 458.5 and 464.2 eV are attributed to the +4 valence state for Ti $2p_{3/2}$ and Ti $2p_{1/2}$, respectively, which further confirms the formation of TiO_2. Additionally, two Gaussian peaks centered at ∼456.6 and ∼461.5 eV were detected, which can be attributed to +3 valence state of Ti $2p_{3/2}$ and Ti $2p_{1/2}$, respectively, confirming the presence of oxygen vacancy in the system.[8] However, no measurable shift in binding energy has been detected in the Ti 2p spectra after HS formation. The relative Ti^{3+}% in the Ti 2p spectra was calculated as 17.4% for TiO_2 NRs and 18.6% for TA32 HS, which shows an indication of enhancement of oxygen vacancy concentration after the HS formation. Figure 3c,d displays the O 1s spectra of TiO_2 and TA32 HS, respectively. Each spectrum follows a long tail in the higher energy region making the spectrum asymmetric, and this tail implies the presence of defects in the sample. The O 1s spectra can be fitted with two symmetric Gaussian peaks, as reported in the literature.[35] The intense peak at ∼529.7 eV is attributed to the TiO_2 crystal lattice, and the other peak at ∼531.1 eV can be assigned to the Ti−O bond ($O_{Ti^{3+}}$). We have calculated the relative $O_{Ti^{3+}}$% in the O 1s spectra for both samples and found it to be 13.16% for pure TiO_2 and 26.34% for TA32 HS, which further proves the increase in the concentration of oxygen vacancy defects in the systems after HS formation. These defect states may also serve as shallow donors and enhance charge transfer at the interface, which in turn improves the overall photocatalytic performance. A summary of the fitting parameters with relative vacancy percentage is shown in Table 2.

Figure 4a shows a comparison of Ag 3d core level XPS spectra of TA32 HS sample before and after photocatalysis.

Table 2. Summary of the Changes in $E_g(1)$ Raman Mode and Relative Area (%) under the Ti^{3+} and O_V Peaks in the XPS Spectra for Different Samples

	Raman mode $E_g(1)$			
sample code	frequency (cm^{-1})	fwhm (cm^{-1})	Ti^{3+} % in Ti $2p_{3/2}$ XPS spectrum	O_v % in O 1s XPS spectrum
TiO_2	146.44	8.16	17.4	13.2
TA11	151.95	17.23		
TA12	147.95	10.11		
TA21	148.70	11.27		
TA23	149.26	12.47		
TA32	152.02	16.27	18.6	26.3

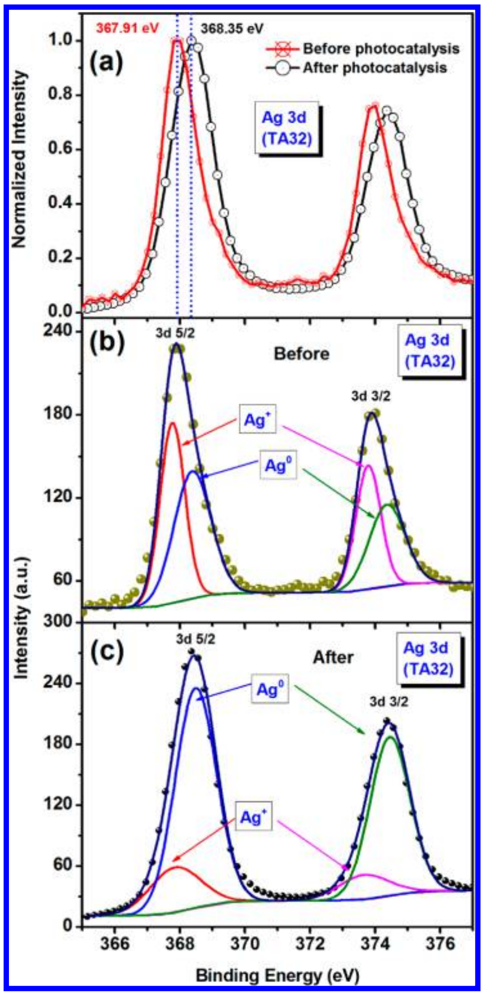

Figure 4. (a) Comparison of Ag 3d core level XPS spectra of sample TA32 before and after photocatalysis. The dotted vertical lines indicate the blue shift of the spectrum after photocatalysis. (b and c) The Gaussian fit of each spectrum with Shirley baseline. Symbols are for experimental data and solid lines are Gaussian fits. The charge state associated with each peak is labeled.

Before photocatalysis, the system exhibits an asymmetry in the higher binding energy range having a Ag $3d_{5/2}$ peak at 367.9 eV, which corresponds to the Ag^+ valence state, and the asymmetry indicates the presence of different valence states of Ag in the HS sample.[38] This may arise due to the following reasons. First, during the photoreduction process, all Ag^+ ions in the solution could not get reduced into metallic Ag^0 and the unsaturated Ag^+ ions are still present in the HS. Second, reverse-spill over is the oxidation mechanism of deposited Ag^0 due to the presence of oxygen ions in the atmosphere.[39]

$$4Ag^0 + O_2^- \rightarrow 2Ag_2O + e^- \tag{1}$$

$$2Ag^0 + O^- \rightarrow Ag_2O + e^- \tag{2}$$

Interestingly, after the photocatalytic reaction, it is observed that the Ag 3d spectrum is more symmetric and the peak shifts to the higher binding energy region having the Ag $3d_{5/2}$ peak at 368.4 eV, which corresponds to the metallic Ag^0 valence state. The symmetry of the line shape in the spectrum indicates that Ag is mostly in a particular valence state, i.e., in Ag^0 state and the Ag^+ state has been reduced.[38] Therefore, it can be concluded that during the photocatalysis the unsaturated Ag^+ ions get reduced into the metallic Ag^0 state since the light source contains some UV photons (wavelength range ~390–800 nm). For a better understanding, each peak of the Ag 3d spectra has been deconvoluted into two symmetric Gaussian peaks, as shown in Figure 4b,c for the HS sample before and after photocatalysis, respectively. It can be noted that the deconvolution of Ag 3d asymmetric spectrum of the TA32 sample before photocatalysis gives the relative percentages of Ag^+ and Ag^0 as 48.17% and 51.83%, respectively. On the other hand, deconvolution of the symmetric Ag 3d spectrum after photocatalysis provides the relative percentages of Ag^+ and Ag^0 as 18.35% and 81.65%, respectively. Thus, the concentration of Ag^0 increases dramatically after photocatalysis. Further, the XPS analyses reveal the oxidation state of Ti and Ag in the HS sample before and after photocatalysis clearly establishing the presence of defects induced in the system.

3.3. Optical Analysis.

3.3.1. UV–vis Absorption Study. In order to measure the optical response of TiO_2 NRs and Ag@TiO_2 heterojunctions, the UV–visible absorption spectra were measured from the diffuse reflectance spectra (DRS) of the powdered samples. The absorbance of a material system is related to the diffuse reflectance (R) by the Kubelka–Munk (K-M) function, $F(R)$, given by

$$F(R) = \frac{(100 - R)^2}{200R} = \frac{\alpha}{S}$$

where α and S represent the absorption and scattering coefficients, respectively, and R is the percentage reflectance of the respective samples. Figure 5a shows the plot of the K-M function of different samples depicting their absorption spectra, and Figure 5b shows the $(F(R)h\nu)^{1/2}$ vs $h\nu$ plot for the calculation of effective band gap (indirect) of the HSs. Extrapolation of the linear portion at $(F(R)h\nu)^{1/2} = 0$ gives the effective band gap of the nanostructures. It is observed that, besides the UV absorption band, the Ag@TiO_2 heterojunctions exhibit a new absorption band in the vis–NIR range having a peak centered at 515–533 nm, as a consequence of the surface plasmon resonance (SPR) absorption of Ag NPs.[40] It can be noted that the position and fwhm of the SPR peak vary with the loading amount of Ag NPs. The peak intensity, position, and broadening depend on the Ag NPs size, density, distribution on the TiO_2 NRs, and also relative percentages of Ag^0 and Ag^+ in the HSs. As is evident from the data, TiO_2 NRs exhibit a sharp absorption edge ~380 nm, and at higher wavelength (visible region), the absorbance is negligibly low. However, when coupled with Ag NPs, Ag@TiO_2 NRs exhibit a strong absorption in the UV–vis–NIR range of 200–850 nm. Though each spectrum exhibits a huge visible light absorption, the HS with Ag and TiO_2 in 3:2 weight ratio (TA32 HS) shows the highest absorption (~1.8 times stronger than other HS samples) in the visible to NIR region. This can be explained as follows. For the TA32 HS, the concentration of $AgNO_3$ in the solution and UV exposure time during the photoreduction synthesis is optimum for the maximum reduction of Ag^+ ions into Ag^0 with uniform and dense distribution on TiO_2 surfaces and comparatively less Ag^+ is present. Thus, the TA32 HS shows extremely uniform size distribution and optimum density of Ag NPs on the TiO_2 surfaces. For the visible light sensitization by Ag NPs, the HSs are expected to have high solar light harvesting and hence enhanced photocatalytic activity in the visible as well as UV and NIR region. Interestingly, the effective band gap of the TiO_2 NRs is reduced after loading with the Ag NPs. Considering the indirect

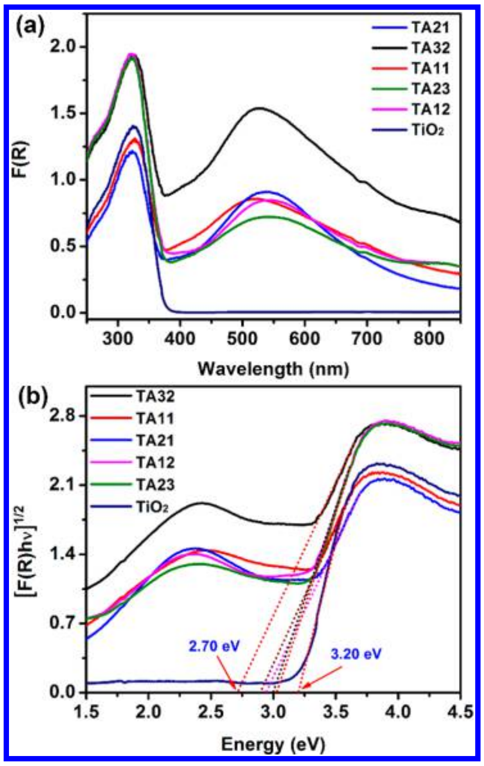

Figure 5. (a) Absorption spectra in terms of Kubelka−Munk plot, $F(R)$, derived from the diffuse reflectance spectra of different samples. (b) Corresponding Tauc plot $[(F(R)h\nu]^{1/2}$ vs $h\nu$ plot considering the indirect band gap nature of the TiO_2 samples. The effective band gap of TiO_2 and its HSs with different Ag content are estimated by the intercept on the x-axis (extrapolated short dashed lines). Note that, all of the HS samples show a strong visible absorption band centered at ∼2.3 eV.

nature of the band gap in the TiO_2 NRs as well as its HSs, the effective band gap of the respective samples has been estimated using the Tauc plot, as shown in Figure 5b.[41] After the decoration of Ag NPs, the effective band gap of TiO_2 NRs has been tuned in the range 2.71−3.03 eV, while the bare TiO_2 NRs shows a band gap of 3.2 eV. The effective band gap of each sample is tabulated in Table 1. The band gap energy modification for the HS samples may be due to the strong coupling between the Ag NPs and TiO_2 NRs. It is noteworthy that, in the case of TA32, the effective band gap is the lowest (2.71 eV), which implies that Ag NPs and TiO_2 NRs HS have large band bending and may have high carrier concentrations at room temperature. This turns out to be extremely beneficial for the efficient visible light photocatalysis by the HSs samples, as discussed later. Note that direct measurement of the absorption spectra of the pristine TiO_2 and TA32 hybrid using an integrating sphere shows results (see Figure S2, Supporting Information) similar that of Figure 5a.

3.3.2. Photoluminescence Study. The nature of the defects, kinetics of charge recombination, and the migration of the photogenerated charge carriers can be explored from the photoluminescence (PL) spectra of the as-grown samples. Figure 6a shows a comparison of steady state PL spectra of pure TiO_2 and the Ag@TiO_2 (TA32) composite with an excitation wavelength of 355 nm. It is observed that introduction of Ag NPs greatly influences the PL intensity of TiO_2 NRs. The PL intensity of the TiO_2 NRs has been observed to be decreased by ∼3 times after the decoration of Ag NPs, though the nature of the PL spectrum remains unchanged. Each PL spectrum is deconvoluted with four Gaussian peaks to elucidate the origin of the broad visible PL. The deconvoluted PL spectra for TiO_2 NRs and TA32 are shown in Figure 6b,c, respectively. The deconvoluted peaks are centered at 433.6 (peak 1), 470.9 (peak 2), 510.3 (peak 3), and 622.8 nm (peak 4) for TiO_2 NRs and at 434.1 (peak 1), 475.7 (peak 2), 529.4 (peak 3), and 603.6 nm (peak 4) for TA32, respectively, as shown in Figure 6b,c. Based on the literature reports, peak 1 is ascribed to self-trapped excitons located at TiO_6 octahedra. Peak 2 coincides with the shallow trap which can be assigned to Ti^{3+} states just below the conduction band, while peak 3 is due to the deep trap state associated with the single electron trapped oxygen vacancy (F^+ center). The PL emission at ∼620 nm (peak 4) may be due to an intrinsic defect.[35] It can be noted that the center of the peaks of the individual bands of sample TA32 and TiO_2 NRs are almost same. However, the intensity of each peak is strongly decreased in sample TA32 as compared to bare TiO_2 NRs, though the HS samples are found to be more defect enriched than the bare TiO_2 NRs, as confirmed from the Raman and XPS analyses. The lower PL intensity signifies reduced recombination owing to the strong coupling between the Ag and TiO_2 and the consequent band bending at the interfaces, which enables stronger electron−hole separation efficiency. Another possible way is the formation of a Schottky junction at the Ag−TiO_2 interface and the buildup of internal electric field directed from TiO_2 to Ag that facilitates the forced as well as fast lane charge transfer from Ag to TiO_2 surface.[30]

3.3.3. Time Resolved Photoluminescence Study. In order to investigate the recombination kinetics of photogenerated charge carriers, time-resolved photoluminescence (TRPL) measurements were performed on bare TiO_2 NRs and TA32 HS with 375 nm laser excitation, and the emission intensity was monitored at 471 nm. The TRPL decay profiles are shown in Figure 6d, which clearly reveals the slower decay kinetics for the HS sample. The PL decay profiles are fitted using a triexponential decay function expressed as follows:

$$I(t) = \sum_{i=1}^{3} A_i e^{(-t/\tau_i)} \tag{3}$$

where τ_i is the lifetime of individual component and A_i is the corresponding amplitude.

The average excited state lifetime (τ_{av}) can be calculated by using the following relationship:[42]

$$\tau_{av} = \frac{\sum_{i=1}^{3} A_i \tau_i^2}{\sum_{i=1}^{3} A_i \tau_i} \tag{4}$$

The details of the time constants (τ_i) and amplitudes (A_i) of bare TiO_2 NRs and TA32 HS are tabulated in the inset of Figure 6d. The triexponential fit suggests that three different states contribute to the TRPL spectra in each sample, which is fully consistent with the steady state PL spectra. It can be noted that the average lifetime (τ_{av}) is considerably increased after Ag loading from 2.62 to 9.81 ns, and consequently, the decay becomes slower in TA32. A longer decay lifetime clearly indicates lower recombination and greater separation efficiency of electron−hole pairs. Thus, the lower recombination of photoexcited electrons and holes will lead to weaker photoluminescence (as shown in Figure 6a). The interfacial charge transfer prolongs the lifetime of the photogenerated charge

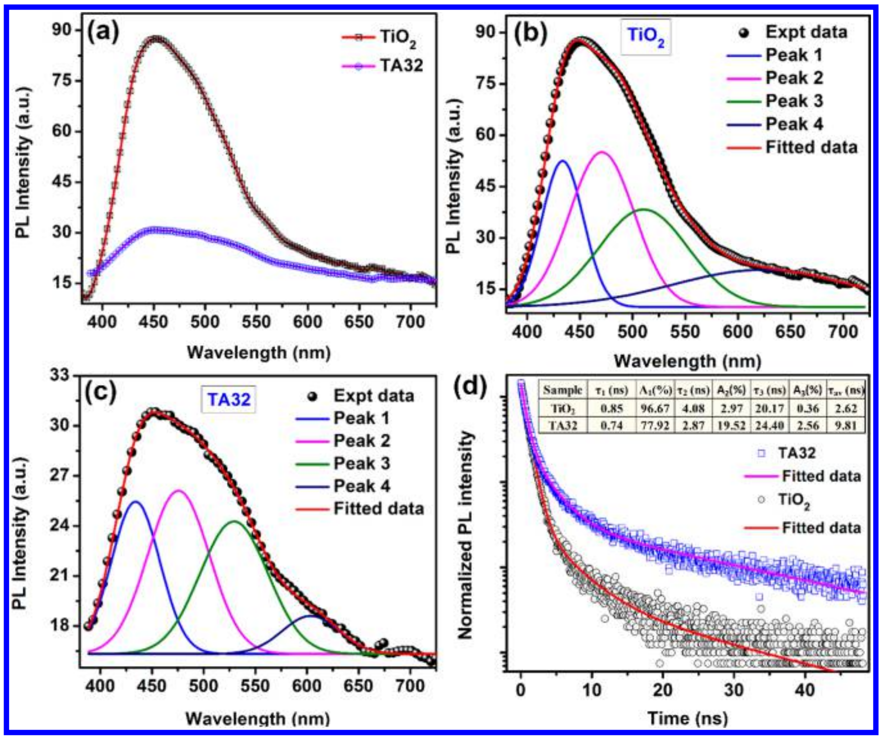

Sample	τ_1 (ns)	A_1(%)	τ_2 (ns)	A_2(%)	τ_3 (ns)	A_3(%)	τ_{av} (ns)
TiO$_2$	0.85	96.67	4.08	2.97	20.17	0.36	2.62
TA32	0.74	77.92	2.87	19.52	24.40	2.56	9.81

Figure 6. (a) Comparison of the PL spectra of TiO$_2$ NRs and Ag@TiO$_2$ HS (TA32) excited with a 355 nm laser. The PL intensity is strongly reduced in the HS sample. (b and c) Gaussian fitted PL spectra of TiO$_2$ NRs and TA32, respectively. (d) A comparison of TRPL spectra of TiO$_2$ NRs and TA32 monitored at 471 nm (emission) with 375 nm excitation. The symbols represent the experimental data, and the solid lines represent the corresponding triexponential fit. The inset shows the details of lifetime of carriers in different samples.

carriers, and thus, higher concentrations of charge carriers are available on the surface of the HS, enhancing visible light photocatalytic performance,[8] as discussed later.

3.4. Photoconductivity Study. To investigate the efficiency of photogenerated carriers and the generation of LSPR induced hot electrons in the Ag NPs anchored to TiO$_2$ HSs and their role in the enhanced visible light photocatalysis, visible light photoresponse measurements with a fixed bias voltage (5 V) have been carried out. The dark current for TA32 is observed to be 35 nA, which is ~4 times higher than that of bare TiO$_2$ NRs (9 nA). This may be due to the higher defect density in the TA32 than that of the bare TiO$_2$ NRs, as confirmed from the PL and XPS analyses. The visible light induced photocurrents of TA32 and bare TiO$_2$ NRs are measured to be 5080 and 990 nA, respectively. It can be noted that the photocurrent of bare TiO$_2$ NRs is ~110 times higher than the dark-current, while it is ~150 times higher in case of TA32 HS, as shown in Figure 7. The enhancement in the photocurrent in bare TiO$_2$ NRs may be due to the generation of electrons in the conduction band of TiO$_2$, which is likely due to the sub band gap defects in TiO$_2$. However, the large enhancement in the photocurrent in TA32 HS is contributed by sub-band gap defects as well as the generation of LSPR induced hot electrons in the Ag side by the strong absorption of visible light. These photogenerated carriers contribute significantly to the enhanced photocatalytic performance of the HS sample.

3.5. Photocatalytic Studies. The hot electrons generated within the Ag NPs and its injection into the TiO$_2$ NRs could be energetic enough to drive photoelectrochemical reactions due to its broad optical absorption. To investigate the photocatalytic efficiency of the samples, we examined the decomposition of RhB in water in the presence of the HS catalysts.

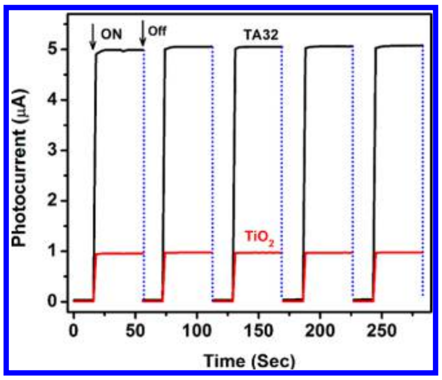

Figure 7. Dark current and photocurrent response of TiO$_2$ and TA32 HS under visible light irradiation on−off process, at a fixed bias voltage 5 V.

3.5.1. Photocatalytic Degradation of RhB. The visible light photocatalytic activity of TiO$_2$ NRs and its heterojunctions was evaluated by measuring the decomposition of RhB as a reference dye under the visible light illumination (details shown in Table 3). In order to compare the efficiencies, the self-decomposition of the dye solution was also examined under identical conditions. Figure 8a shows a comparison of the photodegradation performance of various samples including bare TiO$_2$ NRs and commercial P25 catalyst under visible light irradiation. The HS samples show enhanced photodegradation efficiency as compared to the bare TiO$_2$ NRs. Note that among all of the HS samples, TA32 shows the highest photodegradation efficiency. Figure 8b shows the digital photographs of the change in color of the RhB solution in the presence of

DOI: 10.1021/acs.jpcc.7b05328
J. Phys. Chem. C 2017, 121, 20016−20030

Table 3. Degradation Performance of RhB by Various Catalysts under Visible Light and the Corresponding Pseudo First Order Rate Constants

	maximum degradation (%)			rate constant (min^{-1})	
catalyst name	1st compartment	2nd compartment	total degradation (%)	1st compartment	2nd compartment
without catalyst	12.2		12.2	0.001	
TiO_2 NRs	65.9		65.9	0.008	
TA11	77.9	20.0	97.9	0.023	0.060
TA12	47.6	28.3	75.9	0.009	0.019
TA21	54.5	25.0	79.5	0.012	0.020
TA23	47.8	13.8	61.6	0.009	0.012
TA32	82.9	17.1	100	0.033	0.083
P 25	50.4		50.4	0.007	

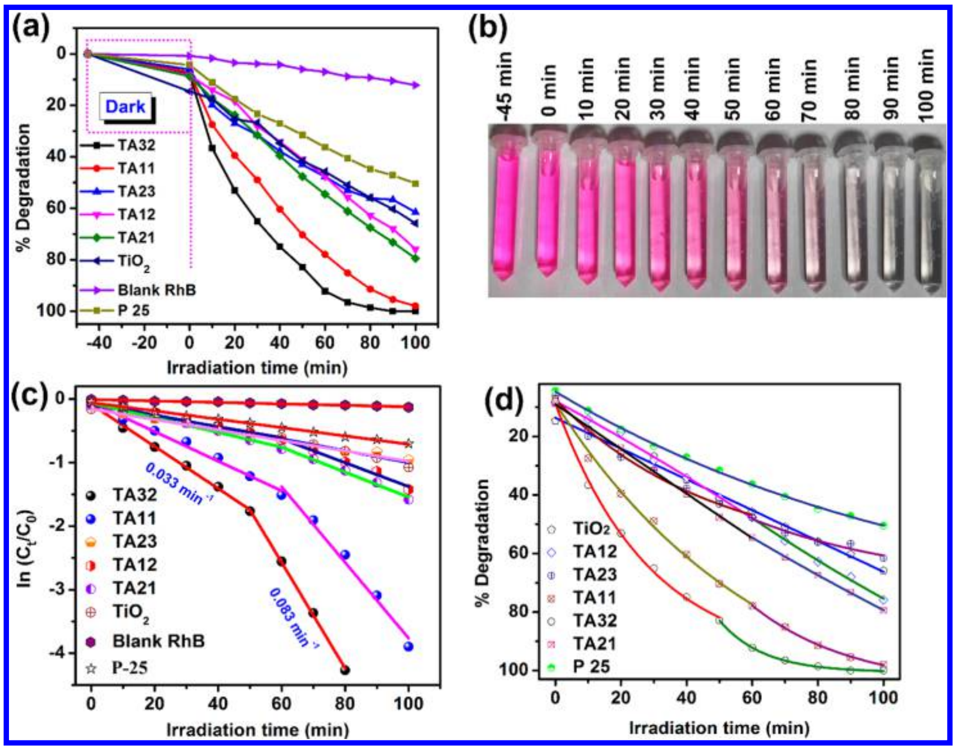

Figure 8. (a) Comparison of the photocatalytic degradation profiles of RhB without and with the presence of different catalyst samples under visible light irradiation. (b) Digital photograph of the degradation induced color change of RhB in the presence of TA32 after exposure to visible light for various time durations. (c) A plot of $\ln\left(\frac{C_t}{C_0}\right)$ vs time for different samples and corresponding linear fitting. (d) Comparison of degradation plots showing exponential decay in two different compartments.

TA32 catalyst as a function of irradiation time due to the photodegradation under visible light irradiation.

Kinetics of the photodegradation of several common organic dyes (methyl orange, methylene blue, Rhodamine-B, etc.) is usually described by a pseudo first order rate kinetics from the Langmuir−Hinshelwood expression: $\ln\left(\frac{C_t}{C_0}\right) = -kt$, where C_0 is the initial concentration of the dye after reaching the adsorption−desorption equilibrium, C_t is the concentration of dye after irradiation time t, and k is the rate constant (min^{-1}).[43] In order to evaluate the rate kinetics, we have plotted the same equation for TiO_2 and Ag@TiO_2 HS samples. Figure 8(c) shows a comparison of the values of $\ln\left(\frac{C_t}{C_0}\right)$ for the respective samples as a function of light irradiation time (t), and Figure 8d shows the percentage degradation of the dye as a function of time fitted with an exponential function. The degradation characteristics could be elucidated by the corresponding linear fit and the value of its slope (k value) is a measure of the rate constant. It is clear from the figure that each $\ln\left(\frac{C_t}{C_0}\right)$ vs time curve of the HS samples can be divided into two decay zones/steps with two distinct linear fits and thus two different k values, whereas the bare TiO_2 NRs and commercial P25 follow a single decay zone with single k values of 0.008 and 0.007 min^{-1}, respectively. It is noteworthy that, in the case of HSs, the degradation rate constant is much higher in the second zone as compared to that of the first zone. Interestingly, for TA32, k (0.083 min^{-1}) is found to be extremely high in the second zone, 1 order of magnitude higher than that of the commercial P25 and about 2.5 fold stronger than that in the first zone (0.033 min^{-1}; see Figure 9b). Thus, in comparison to bare TiO_2 NRs, this k value is about 10 times stronger in the second zone and 4 times stronger in the first zone. Considering the

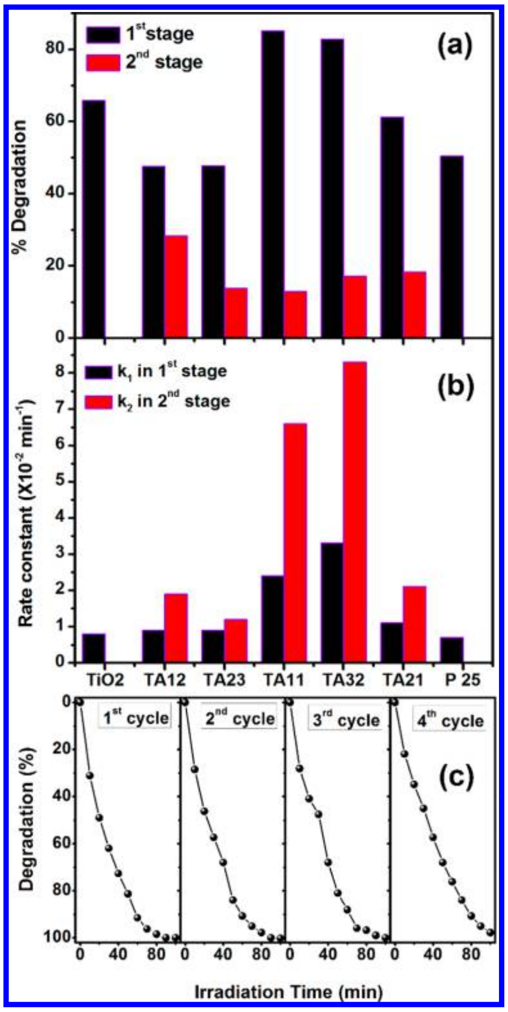

Figure 9. (a) Comparison of the photodegradation percentages of RhB in the first and second compartment of degradation calculated for different samples and (b) the associated rate constants. (c) Cyclic stability of TA32 as a visible light photocatalyst for four cycles considering RhB as a model dye.

visible light irradiation, the high rate constant of 0.083 min^{-1} of the HS sample is very significant. Note that most of the reported k values under visible light irradiation are about 1 order of magnitude lower than our result.[44] In our study, the degradation rate constant in the second stage for the TA32 sample is ∼12 times stronger than that of the commercial P25. It is observed that a large fraction of total dye is decomposed in the first zone of degradation and a lower fraction in the second zone (see Figure 9a). Note that our data cannot be fitted by a single or biexponential decay behavior. We observed that, for all of the HSs, the degradation rate is much faster in the second zone than the first zone. In both the zones, TA11 and TA32 show the maximum overall photodegradation efficiency. Prior to the illumination of visible light, the catalysts were well dispersed in the dye solution and magnetically stirred for 45 min in dark. This established the equilibrium between dye molecules and the catalyst surfaces. After reaching the adsorption/desorption equilibrium (at 0 min of irradiation), we have observed that ∼85% and ∼92% of dye are still present in the solution of TiO_2 and HSs, respectively. Thus, it can be noted that, after the decoration of Ag NPs, the dye adsorption by TiO_2 NRs has been decreased from 15% to 8%. This may be due to the presence of pores on TiO_2 surface into which the dye molecules get adsorbed. However, after the formation of HSs, these pores have been filled by the Ag NPs leading to the lower adsorption efficiency.

Scherr et al.[45] studied the degradation kinetics of bio compound Estrone-3-sulfate (E1-3S), formed in the kidneys of pregnant cattle, with "single first-order exponential decay model" and "two-compartment first-order biexponential decay model", assuming no back conversion, no influence of sorption on the degradation, and no altering due to microbial growth. These models can be described mathematically as follows:

$$\text{single first order (SFO):} \quad C_t = C_0 e^{-k_1 t} \tag{5}$$

double first order in parallel (DFOP):

$$C_t = C_0[g e^{-k_1 t} + (1-g) e^{-k_2 t}] \tag{6}$$

where t is the time of irradiation, k_1 and k_2 are the degradation rate constants (min^{-1}) in first stage and second stage, respectively, C_0 is the initial concentration of parent compound, C_t is the total concentration of parent compound at time t, and g is the fraction of C_0 applied to stage 1 of the DFOP model. We noticed that the single first order exponential decay model is not valid in our case, as we have observed two different degradation zones with two distinct rate constants. According to the DFOP model, degradation takes place in two stages: rapid degradation in the first stage as the microorganisms have easy access to the compound, whereas in the second stage, degradation is rather slow and the compound is expected to be adsorbed to soil particles or to be located in micropores within the soil matrix. The speed at which the parent compound is transformed is expressed as degradation rate constant (k_1, in the first stage, and k_2, in the second stage) and usually $k_1 > k_2$. However, our data could not be fitted either with the SFO or the DFOP model (see Figure 11a,b).

Interestingly, in the present case, the degradation process of all HS samples follows a sequential decay model in contrast to the parallel process model of DFOP. This sequential process can be mathematically described as

$$C_t = C_0 e^{-k_1 t} \quad \text{up to } 0 \le t \le t_1 \tag{7}$$

$$C'_t = C_{t_1} e^{-k_2(t-t_1)} = C_0 e^{-k_1 t_1} e^{-k_2(t-t_1)} \quad t > t_1 \tag{8}$$

where C_0 is the concentration of the parent dye prior to the irradiation and C_t and C'_t are the concentration of the dye after time t of irradiation in stages 1 and 2, respectively. k_1 and k_2 are the degradation rate constants (in min^{-1}) in first and second stages, respectively. t_1 is the irradiation time up to which the first compartment of degradation extends (eq 7) and beyond which the second compartment of degradation starts (eq 8). Herein, the whole degradation process occurs in two different compartments/stages separately, where the first compartment runs in the irradiation time range $0 \le t \le t_1$ and afterward ($t > t_1$) the second compartment extends. The limiting time t_1 is found to be ∼60 min for all of the HS samples except for the optimized HS, TA32 (50 min). It can also be noted that a higher fraction of dye is being decomposed in the first zone and lesser fraction in the second zone (Figure 9a), though the degradation rate is higher in the second compartment. More details of the physical mechanism behind the sequential model are discussed later.

3.5.2. Cyclic Stability of the Photocatalysts. To evaluate the performance stability of the Ag@TiO_2 HS as visible light photocatalyst, each sample was repeatedly used for four cycles

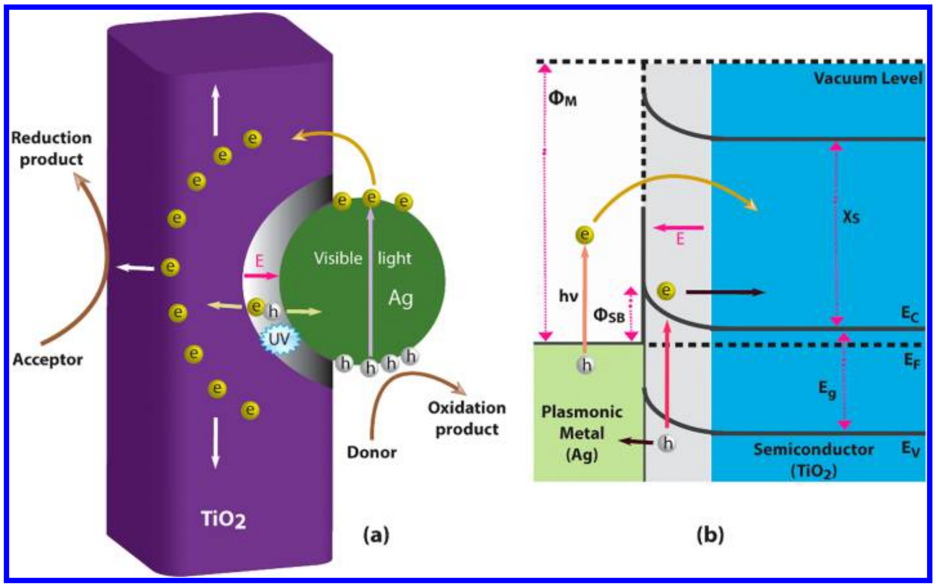

Figure 10. (a) Schematic representation of Ag@TiO_2 NRs HS showing the generation of hot electrons, their separation, and participation in the photocatalysis. (b) A schematic illustration of the energy band diagram of TiO_2 in the presence of Ag NP, where a Schottky barrier is formed between the two, where vacuum level is the vacuum energy level, Φ_M is the work function of the Ag NP, Φ_{SB} is the Schottky barrier height, and χ_S is the electron affinity of TiO_2. In the proposed mechanism, the decaying SPR excites "hot" electrons in the Ag nanoparticles that possess enough energy to overcome the Schottky barrier and inject into the TiO_2.

after separation from dye solution by centrifugation followed by filtration. For this study, TA32 has been chosen as the model HS catalyst as it shows the highest photo degradation capability, as shown in Figure 8a. The TA32 photocatalyst exhibits extremely stable photocatalytic activity under visible light irradiation, as shown in Figure 9c, and there is no obvious change in the photo degradation efficiency after four cycles of use. After the first cycle of photocatalysis, the reduced Ag^+ ions may get again oxidized by the reverse spillover effect,[39] and additionally after the migration of hot electrons through the interface of heterojunctions of Ag and TiO_2, the Ag NPs get positively charged and thus have a higher tendency to be oxidized in ambient conditions. Thus, the Ag decorated TiO_2 NRs are found to be extremely stable photocatalysts with the potential for commercial applications. Our results demonstrate the superiority of the Ag@TiO_2 HS over the bare TiO_2 NRs for its advanced application in environmental cleaning.

3.5.3. Mechanism of Enhanced Visible Light Photocatalytic Activity. In the present work, the band gap as well as the absorption range of TiO_2 NRs are tuned with the decoration of Ag NPs so that it can absorb an extended spectrum of solar light. In the case of HS samples, the Ag NPs are strongly coupled with the TiO_2 lattice, and due to the synergetic effect and band bending, the HS shows strong absorption of vis−NIR light and efficient charge transfer at the interface.[8] As a result, the visible light photocatalytic activity of TiO_2 NRs HS has been found to be enhanced enormously. Possible mechanisms including additional boosting factors behind the enhanced visible light photocatalysis are discussed below.

Figure 10a,b shows a schematic of the vacancy rich n-type TiO_2 NR coupled with an Ag NP and a schematic illustration of the energy band diagram of Ag@TiO_2 HS, respectively. The presence of Ag NP on TiO_2 results in a Schottky barrier with a space charge region in the TiO_2 region, which builds up an internal electric field E pointing from the TiO_2 to the Ag.[30] Such an internal field forces the electron−hole pairs generated in the space charge region (TiO_2 side) to move in opposite directions separating electrons and holes and suppressing their easy recombination in TiO_2. A noteworthy feature of plasmonic photocatalysis is that the Ag NP is able to absorb visible light and drives coherent collective oscillation of electrons, which in turn generates electrons with high kinetic energy in the range 1−3 eV.[26] With visible light illumination, the Ag NP on the surface of TiO_2 NR absorbs light, and consequently the LSPR occurs. The excited plasmons can decay in the femtosecond time scale through two different processes: radiatively via re-emitting the photons and nonradiatively via transferring the gathered energy to electrons in the conduction band of the material. Thus, the nonradiative energy transfer produces highly energetic electrons, also known as "hot electrons" at the Ag surface. Generally, the energy of these hot electrons is greater than the Schottky barrier height ($h\nu > \varphi_{SB}$) and can escape easily from the Ag surface and are collected by the TiO_2 NRs, since TiO_2 is a good electron-accepting metal oxide because of the high density of states in its conduction band.[26] Further, the internal electric field (E) assists their separation forcing the electron to move to the TiO_2 region and the hole to the Ag region and thus prevents the recombination. After separation of photoinduced charge carriers, the TiO_2 surface near the Ag NPs is crowded by the electrons. Having a 1D structure, TiO_2 NR possess low axial resistance, and thus the electrons can diffuse through their length making their lifetime further lengthened, as confirmed by PL and TRPL analyses (see Figure 10a). Thus, the electrons and holes available at the surface of Ag@TiO_2 HS shown in the illustrated figure react with the adsorbed O_2 and H_2O molecules and eventually form highly active super oxide and hydroxyl radicals, which are strong reducing and oxidizing agents, respectively. These radicals are primarily responsible for the efficient degradation of dye under visible light irradiation.[8,46]

Further, our results showed that after incorporation of the Ag NPs on the TiO_2 NRs, the concentration of oxygen vacancy defects was increased, as concluded from Raman and XPS

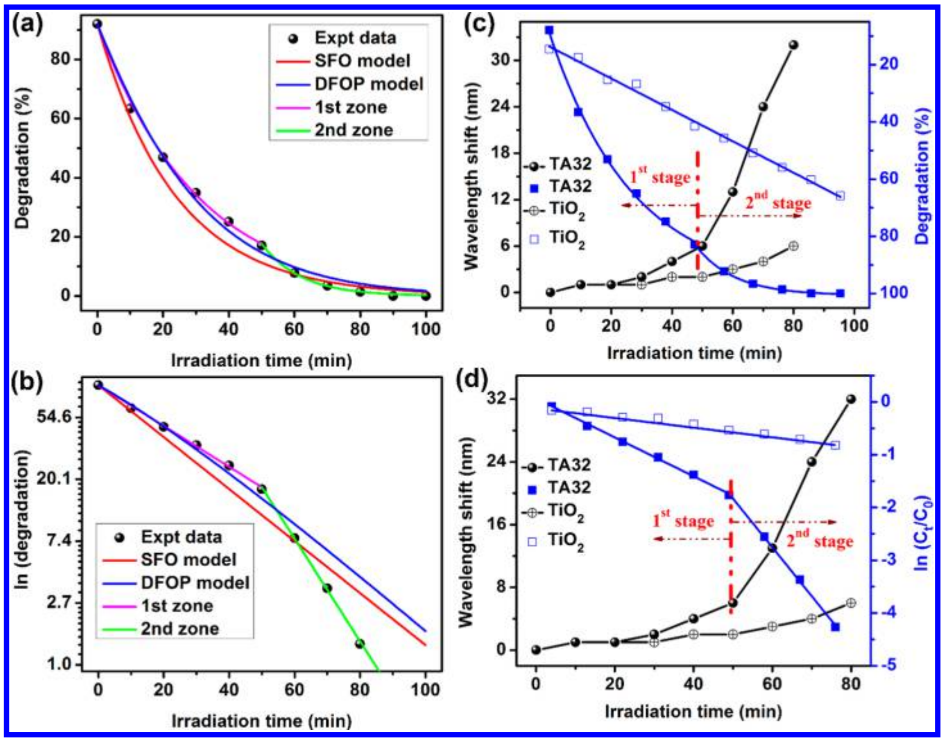

Figure 11. Percentage degradation of RhB under visible light illumination (a) and a plot of ln(degradation) vs irradiation time (b), fitted with SFO, DFOP, and sequential model. (c) A plot of degradation (%) vs irradiation time (min) for TiO_2 and TA32 samples (blue *Y* axis) and corresponding wavelength shifts in the absorbance band of RhB (black *Y* axis). The degradation vs irradiation time curves have been fitted with exponential to identify the distinct stages of degradation. (d) A plot of $\ln\left(\frac{C_t}{C_0}\right)$ vs irradiation time (min) for TiO_2 and TA32 samples (blue *Y* axis) and corresponding wavelength shifts in the absorbance band of RhB (black *Y* axis). The $\ln\left(\frac{C_t}{C_0}\right)$ vs irradiation time curves have been fitted with linear equations to identify the distinct stages of degradation.

analyses. The TA32 HS showed the maximum blue shift in the Raman spectra, indicating the optimum value of oxygen vacancy defects. The defects are known to increase the free carrier density in the TiO_2 surface, which increases the probability of superoxide radical formation at the surface and hence the improved photocatalytic efficiency. It also serves as a shallow trap and improves charge transfer at the interface between the Ag and TiO_2. The UV light generated (TiO_2) electrons migrate to shallow traps and reduce Ti^{4+} into Ti^{3+} state through the following pathway:[47]

$$TiO_2 \xrightarrow{h\nu(\text{UV})} e^-_{CB} + h^+_{VB}$$

$$e^-_{CB} + Ti^{4+} \rightarrow Ti^{3+}(\text{trapped electron})$$

For the visible light irradiation, the TiO_2 does not get excited directly, but the hot electrons generated at the Ag surface can excite it.[47]

$$\text{Ag NP} \xrightarrow{h\nu(\text{vis})} e^-(\text{hot})$$

$$e^-(\text{hot}) \xrightarrow{\text{after migration}} e^-_{CB} + \xrightarrow{Ti^{4+}} Ti^{3+}(\text{trapped electron})$$

Thus, the defect-assisted charge carrier generation and its separation plays an important role as one of the boosting factors for enhanced photocatalytic efficiency.

Further, it has been reported that the photodegradation rate depends on the relative concentration of dye and catalyst present in the solution. For example, a lower dye to catalyst ratio gives the higher degradation rate. In the first stage of degradation, the full amount of dye (0.5 mg) takes part, which represents a higher ratio of dye to catalyst. Next, in the second stage of degradation, the remaining amount of dye was involved and as the maximum fraction of total dye is being degraded in the first zone, the dye to catalyst ratio is very small in the second zone of degradation. For example, in case of TA32 sample, the dye to catalyst ratio is 0.025 in the first compartment and 0.0035 in the second compartment. Thus, in the first compartment the dye to catalyst ratio is more than seven times (7.14) that in the second compartment. In the first compartment, 20 mg of catalyst was applied to entire RhB in the solution, but in the second compartment almost the same amount of catalyst is applied to a much less amount of dye (~15% for TA32). Thus, the lower dye to catalyst ratio may be partly responsible for the faster degradation in the second compartment of degradation.

Interestingly, with irradiation time, not only the absorption peak intensity of RhB centered at ~554 nm (the most intense peak) decreases but also there is a blue shift of the peak position (see Figure S3, Supporting Information). This shift is quite small for bare TiO_2 for the entire period (only ~6 nm shift after 80 min of irradiation), and it is significantly large (~35 nm) for the HS samples. It is noteworthy that, in the first compartment of degradation, the blue shift is relatively small, while it changes dramatically in the second compartment of degradation and is measured to be very large as shown in Figure 11c,d. The blue shift of the absorption peak is generally caused by de-ethylation of RhB (*N*,*N*,*N*′,*N*′-tetraethylated rhodamine) because of the attack by the active oxygen species on the N-ethyl group. The N-de-ethylation is a process of stepwise removal of ethyl group (C_2H_5) attached to the nitrogen atom of RhB molecule during irradiation. Detailed studies by Li et al.[48] and Sridharan et al.[49] showed the stepwise de-ethylation of RhB under the visible light irradiation and formation of rhodamine as the final product. The N-de-ethylation process could be initiated by both valence band hole and conduction band electron in the HSs. The reaction steps are given below:

$$\mathrm{HS} + \mathrm{RhB} \rightarrow \mathrm{RhB}_{\mathrm{Adsorbed}}$$

$$\mathrm{RhB}_{\mathrm{Adsorbed}} \xrightarrow{h\nu} \mathrm{RhB}^{*}_{\mathrm{Adsorbed}}$$

$$\mathrm{RhB}^{*}_{\mathrm{Adsorbed}} + \mathrm{HS} \rightarrow \mathrm{RhB}^{+}_{\mathrm{Adsorbed}} + \mathrm{HS(e^{-})}$$

$$\mathrm{HS(e^{-})} + \mathrm{O_2} \rightarrow \mathrm{HS} + \bullet\mathrm{O_2^{-}}$$

$$\mathrm{HS} \xrightarrow{h\nu} \mathrm{h^{+}} + \mathrm{e^{-}}$$

$$\mathrm{RhB}_{\mathrm{Adsorbed}} + \mathrm{HS(h^{+})} \rightarrow \mathrm{RhB^{+}} + \mathrm{HS}$$

$$\mathrm{RhB^{+}} \xrightarrow{\text{N-de-ethylation}} \text{de-ethylated intermediates} \\ \rightarrow \text{degraded product}$$

In the present study, the small shift of the absorption peak (554 nm) for the bare TiO_2 after light illumination indicates a negligibly slow N-de-ethylation process and relatively dominant chromophore structure degradation. In the case of HSs, up to certain time of irradiation, a very small blue shift in the absorption peak of RhB implies that the degradation occurs mainly due to the adsorption and chromophore ring structure destruction but not due to the N-de-ethylation. However, after a certain time of irradiation (50 min for TA32), the N-de-ethylation process dominates over the other degradation processes and occurs very quickly with the irradiation, as shown in Figure 10c,d. After 60 min, the absorption peak of RhB detected at ∼539 nm can be assigned to *N,N,N′*-triethylated rhodamine[49] and after 80 min at ∼522 nm for *N,N′*-diethylated rhodamine.[49] Figure 11c shows a plot of degradation (%) vs irradiation time (min) for TiO_2 and TA32 samples (see right-hand side *Y* axis) and corresponding wavelength shifts in the absorbance band of RhB (see left-hand side *Y* axis). The degradation curves have been fitted with exponential decay functions to identify the distinct stages of degradation. Figure 11d depicts a plot of $\ln\left(\frac{C_t}{C_0}\right)$ vs irradiation time (min) for TiO_2 and TA32 samples (see RHS *Y* axis) and corresponding wavelength shifts in the absorbance band of RhB (see LHS *Y* axis). The $\ln\left(\frac{C_t}{C_0}\right)$ vs irradiation time curves have been fitted linearly to identify the distinct stages of degradation. It is clear from Figure 11 that, for up to 50 min of irradiation (for TA32), the degradation curve follows a pseudo first order decay, beyond which the N-de-ethylation process dominates and the shift of the resultant absorption peak of RhB becomes very large and significant. This results in a separate degradation exponential starting at 50 min and thus the two separate degradation rate constants.

Another important mechanism that contributes to the two distinct compartments of photodegradation and the enhanced photocatalysis in the second stage of degradation is the reduction process of Ag^+ ions into metallic Ag^0 NPs during photocatalysis. The concentration of Ag^+ ions in the solution may be high enough and during the photoreduction process the UV irradiation time may be insufficient so that some fraction of the Ag^+ ions are not reduced into metallic Ag NPs. XPS analysis before photocatalysis showed that 48.17% of the Ag is present in the Ag^+ ion form. Thus, the plasmonic effect during the photocatalysis is expected only from the 51.83% of Ag NPs and the remaining 48.17% of Ag^+ ions do not contribute to the plasmonic effect. During the photocatalysis process, the light irradiation transforms the Ag^+ ions into Ag^0 NPs with a very slow rate as the irradiation spectrum contains a small portion of UV light (>390 nm). After a certain irradiation time, the amount of Ag^0 NPs in the solution increases (81.65% Ag^0 NPs after photocatalysis) and consequently the plasmonic effect enhances and also the dye to catalyst ratio decreases by ∼10 times as compared to the initial value. Thus, due to the combined effects of photoreduction of Ag and rapid rate of N-de-ethylation process, the degradation rate was enhanced enormously after a certain time of irradiation and thus the calculated rate constant. Thus, two distinct degradation rate constants were observed in two different irradiation time zones, which were named as first and second compartments of the degradation. Note that our data could not be fitted with the SFO and DFOP models of eqs 5 and 6, as shown in Figure 11a,b. However, it fits very well to the sequential model represented by eqs 7 and 8 (see Figure 11a,b), as simulated by Mathematica. Thus, in the present case, a two stage degradation process is most appropriate. Interestingly, photocatalytic degradation studies reported by Cheng et al.,[31] Chen et al.,[32] Wang et al,.[33] and Cui et al.[34] using Ag, Ag_2O, and AgBr incorporated TiO_2 nanostructures assumed the pseudo first order rate kinetics with single rate constant. However, the presented data is not fully consistent with the single exponential decay due to the poor fitting, and the data could be fitted better with a sequential rate process, as discussed in this manuscript.

4. CONCLUSION

In summary, TiO_2 NRs and their defect enriched HSs with Ag NPs are prepared by a solvothermal method followed by a photoreduction method. Uniform decoration of monodisperse Ag NPs on TiO_2 NRs has been evidenced by FESEM, HRTEM, XRD, and XPS analyses, and the effects of the NPs on the stoichiometry, band structure, and optical absorbance of TiO_2 have been elucidated. A photoconductivity study reveals a much higher photo-to-dark current ratio for the TA32 HS sample as compared to that of the pristine TiO_2 sample. The photocatalytic results demonstrate the superior photocatalytic activity of HS samples as compared to the commercial P25 catalyst as well as the individual components. We have shown that the dye degradation for all of the HS samples possesses two distinct decay compartments in time and thus two separate degradation rate constants, which cannot be fitted with SFO or DFOP decay models. In the second compartment of degradation, the rate constant (k_2 = 0.083 min^{-1} for TA32) is much higher than that in the first compartment (k_1 = 0.033 min^{-1} for TA32). Our results are explained in terms of a sequential decay process with exponential decay in each stage. The higher value of k_2 than k_1 has been explained on the basis of ultrafast N-de-ethylation of RhB and enhanced plasmonic effect on Ag NPs and hence the more hot electron generation and their easy injection into the TiO_2 surface. These results are very significant, and it may provide valuable insights into the design and understanding of advanced photocatalytic material with noble metal NPs and enhanced photocatalytic activity with multi rate constants.

■ ASSOCIATED CONTENT

Ⓢ Supporting Information

The Supporting Information is available free of charge on the ACS Publications website at DOI: 10.1021/acs.jpcc.7b05328.

> Size distribution of Ag NPs in different HSs and their log-normal fitting, UV−vis absorption spectra of TiO_2 and TA32 HS, and the shift of the absorption peak of RhB under visible light illumination. (PDF)

■ AUTHOR INFORMATION

Corresponding Author

*E-mail: giri@iitg.ernet.in.

ORCID

P. K. Giri: 0000-0003-2020-4249

Notes

The authors declare no competing financial interest.

■ ACKNOWLEDGMENTS

We acknowledge the financial support from CSIR (Grant No. 03(1270)/13/EMR-II) and MEITY (Grant No. 5(9)/2012-NANO (VOL-II)) for carrying out part of this work. Central Instruments Facility, I.I.T. Guwahati is acknowledged for providing the Raman, TEM, and FESEM facilities. We thank Prof. M. Fujii, Kobe University, Japan for help in the XPS measurement.

■ REFERENCES

(1) Hoffmann, M. R.; Martin, S. T.; Choi, W.; Bahnemann, D. W. Environmental Applications of Semiconductor Photocatalysis. *Chem. Rev.* **1995**, *95*, 69.

(2) Chen, X.; Mao, S. S. Titanium Dioxide Nanomaterials: Synthesis, Properties, Modifications, and Applications. *Chem. Rev.* **2007**, *107*, 2891−2959.

(3) Fujishima, A.; Honda, K. Electrochemical Photolysis of Water at a Semiconductor Electrode. *Nature* **1972**, *238*, 37−38.

(4) Linsebigler, A. L.; Lu, G.; Yates, J. T. Photocatalysis on Tio2 Surfaces: Principles, Mechanisms, and Selected Results. *Chem. Rev.* **1995**, *95*, 735−758.

(5) Liang, Y.-C.; Wang, C.-C.; Kei, C.-C.; Hsueh, Y.-C.; Cho, W.-H.; Perng, T.-P. Photocatalysis of Ag-Loaded Tio2 Nanotube Arrays Formed by Atomic Layer Deposition. *J. Phys. Chem. C* **2011**, *115*, 9498.

(6) O'Regan, B.; Gratzel, M. A Low-Cost, High-Efficiency Solar Cell Based on Dye-Sensitized Colloidal Tio2 Films. *Nature* **1991**, *353*, 737−740.

(7) Zhang, H.; Lv, X.; Li, Y.; Wang, Y.; Li, J. P25-Graphene Composite as a High Performance Photocatalyst. *ACS Nano* **2010**, *4*, 380.

(8) Paul, K. K.; Ghosh, R.; Giri, P. K. Mechanism of Strong Visible Light Photocatalysis by Ag 2 O-Nanoparticle-Decorated Monoclinic Tio 2 (B) Porous Nanorods. *Nanotechnology* **2016**, *27*, 315703.

(9) Shah, Z. H.; Wang, J.; Ge, Y.; Wang, C.; Mao, W.; Zhang, S.; Lu, R. Highly Enhanced Plasmonic Photocatalytic Activity of Ag/Agcl/Tio2 by Cuo Co-Catalyst. *J. Mater. Chem. A* **2015**, *3*, 3568−3575.

(10) Binas, V.; Venieri, D.; Kotzias, D.; Kiriakidis, G. Modified Tio2 Based Photocatalysts for Improved Air and Health Quality. *J. f Materiomics* **2017**, *3*, 3.

(11) Asahi, R.; Morikawa, T.; Ohwaki, T.; Aoki, K.; Taga, Y. Visible-Light Photocatalysis in Nitrogen-Doped Titanium Oxides. *Science* **2001**, *293*, 269.

(12) Burda, C.; Lou, Y.; Chen, X.; Samia, A. C. S.; Stout, J.; Gole, J. L. Enhanced Nitrogen Doping in Tio2 Nanoparticles. *Nano Lett.* **2003**, *3*, 1049−1051.

(13) Duonghong, D.; Borgarello, E.; Graetzel, M. Dynamics of Light-Induced Water Cleavage in Colloidal Systems. *J. Am. Chem. Soc.* **1981**, *103*, 4685−4690.

(14) Naldoni, A.; Allieta, M.; Santangelo, S.; Marelli, M.; Fabbri, F.; Cappelli, S.; Bianchi, C. L.; Psaro, R.; Dal Santo, V. Effect of Nature and Location of Defects on Bandgap Narrowing in Black Tio2 Nanoparticles. *J. Am. Chem. Soc.* **2012**, *134*, 7600−7603.

(15) Santara, B.; Giri, P. K.; Imakita, K.; Fujii, M. Evidence for Ti Interstitial Induced Extended Visible Absorption and near Infrared Photoluminescence from Undoped Tio2 Nanoribbons: An in Situ Photoluminescence Study. *J. Phys. Chem. C* **2013**, *117*, 23402−23411.

(16) Sarina, S.; Zhu, H.; Jaatinen, E.; Xiao, Q.; Liu, H.; Jia, J.; Chen, C.; Zhao, J. Enhancing Catalytic Performance of Palladium in Gold and Palladium Alloy Nanoparticles for Organic Synthesis Reactions through Visible Light Irradiation at Ambient Temperatures. *J. Am. Chem. Soc.* **2013**, *135*, 5793−5801.

(17) Zhao, Z.; Zhang, X.; Zhang, G.; Liu, Z.; Qu, D.; Miao, X.; Feng, P.; Sun, Z. Effect of Defects on Photocatalytic Activity of Rutile Tio2 Nanorods. *Nano Res.* **2015**, *8*, 4061−4071.

(18) Mondal, S.; Basak, D. Defect Controlled Tuning of the Ratio of Ultraviolet to Visible Light Emission in Tio2 Thin Films. *J. Lumin.* **2016**, *179*, 480−486.

(19) Daghrir, R.; Drogui, P.; Robert, D. Modified Tio2 for Environmental Photocatalytic Applications: A Review. *Ind. Eng. Chem. Res.* **2013**, *52*, 3581−3599.

(20) Liu, R.; Wang, P.; Wang, X.; Yu, H.; Yu, J. Uv- and Visible-Light Photocatalytic Activity of Simultaneously Deposited and Doped Ag/Ag(I)-Tio2 Photocatalyst. *J. Phys. Chem. C* **2012**, *116*, 17721−17728.

(21) Pernik, D. R.; Tvrdy, K.; Radich, J. G.; Kamat, P. V. Tracking the Adsorption and Electron Injection Rates of Cdse Quantum Dots on Tio2: Linked Versus Direct Attachment. *J. Phys. Chem. C* **2011**, *115*, 13511−13519.

(22) Bian, Z.; Tachikawa, T.; Zhang, P.; Fujitsuka, M.; Majima, T. Au/Tio2 Superstructure-Based Plasmonic Photocatalysts Exhibiting Efficient Charge Separation and Unprecedented Activity. *J. Am. Chem. Soc.* **2014**, *136*, 458−465.

(23) Lee, H.; Lee, Y. K.; Hwang, E.; Park, J. Y. Enhanced Surface Plasmon Effect of Ag/Tio2 Nanodiodes on Internal Photoemission. *J. Phys. Chem. C* **2014**, *118*, 5650−5656.

(24) Zhang, Z.; Wang, Z.; Cao, S.-W.; Xue, C. Au/Pt Nanoparticle-Decorated Tio2 Nanofibers with Plasmon-Enhanced Photocatalytic Activities for Solar-to-Fuel Conversion. *J. Phys. Chem. C* **2013**, *117*, 25939−25947.

(25) Barad, H.-N.; Ginsburg, A.; Cohen, H.; Rietwyk, K. J.; Keller, D. A.; Tirosh, S.; Bouhadana, Y.; Anderson, A. Y.; Zaban, A. Hot Electron-Based Solid State Tio2|Ag Solar Cells. *Adv. Mater. Interfaces* **2016**, *3*, 1500789.

(26) Clavero, C. Plasmon-Induced Hot-Electron Generation at Nanoparticle/Metal-Oxide Interfaces for Photovoltaic and Photocatalytic Devices. *Nat. Photonics* **2014**, *8*, 95−103.

(27) Wang, P.; Huang, B.; Qin, X.; Zhang, X.; Dai, Y.; Wei, J.; Whangbo, M.-H. Ag@Agcl: A Highly Efficient and Stable Photocatalyst Active under Visible Light. *Angew. Chem., Int. Ed.* **2008**, *47*, 7931−7933.

(28) Yu, J.; Dai, G.; Huang, B. Fabrication and Characterization of Visible-Light-Driven Plasmonic Photocatalyst Ag/Agcl/Tio2 Nanotube Arrays. *J. Phys. Chem. C* **2009**, *113*, 16394−16401.

(29) Awazu, K.; Fujimaki, M.; Rockstuhl, C.; Tominaga, J.; Murakami, H.; Ohki, Y.; Yoshida, N.; Watanabe, T. A Plasmonic Photocatalyst Consisting of Silver Nanoparticles Embedded in Titanium Dioxide. *J. Am. Chem. Soc.* **2008**, *130*, 1676−1680.

(30) Zhang, X.; Chen, Y. L.; Liu, R.-S.; Tsai, D. P. Plasmonic Photocatalysis. *Rep. Prog. Phys.* **2013**, *76*, 046401.

(31) Cheng, B.; Le, Y.; Yu, J. Preparation and Enhanced Photocatalytic Activity of Ag@Tio2 Core−Shell Nanocomposite Nanowires. *J. Hazard. Mater.* **2010**, *177*, 971−977.

(32) Chen, L.; Yang, S.; Hao, B.; Ruan, J.; Ma, P.-C. Preparation of Fiber-Based Plasmonic Photocatalyst and Its Photocatalytic Performance under the Visible Light. *Appl. Catal., B* **2015**, *166–167*, 287–294.

(33) Wang, Y.; Liu, L.; Xu, L.; Meng, C.; Zhu, W. Ag/Tio2 Nanofiber Heterostructures: Highly Enhanced Photocatalysts under Visible Light. *J. Appl. Phys.* **2013**, *113*, 174311.

(34) Cui, Y.; Ma, Q.; Deng, X.; Meng, Q.; Cheng, X.; Xie, M.; Li, X.; Cheng, Q.; Liu, H. Fabrication of Ag-Ag2o/Reduced Tio2 Nanophotocatalyst and Its Enhanced Visible Light Driven Photocatalytic Performance for Degradation of Diclofenac Solution. *Appl. Catal., B* **2017**, *206*, 136–145.

(35) Santara, B.; Giri, P. K.; Imakita, K.; Fujii, M. Evidence of Oxygen Vacancy Induced Room Temperature Ferromagnetism in Solvothermally Synthesized Undoped Tio2 Nanoribbons. *Nanoscale* **2013**, *5*, 5476.

(36) Choi, H. C.; Jung, Y. M.; Kim, S. B. Size Effects in the Raman Spectra of Tio2 Nanoparticles. *Vib. Spectrosc.* **2005**, *37*, 33–38.

(37) Balaji, S.; Djaoued, Y.; Robichaud, J. Phonon Confinement Studies in Nanocrystalline Anatase-Tio2 Thin Films by Micro Raman Spectroscopy. *J. Raman Spectrosc.* **2006**, *37*, 1416–1422.

(38) Murray, B. J.; Li, Q.; Newberg, J. T.; Menke, E. J.; Hemminger, J. C.; Penner, R. M. Shape- and Size-Selective Electrochemical Synthesis of Dispersed Silver(I) Oxide Colloids. *Nano Lett.* **2005**, *5*, 2319.

(39) Albiter, E.; Valenzuela, M. A.; Alfaro, S.; Valverde-Aguilar, G.; Martínez-Pallares, F. M. Photocatalytic Deposition of Ag Nanoparticles on Tio2: Metal Precursor Effect on the Structural and Photoactivity Properties. *J. Saudi Chem. Soc.* **2015**, *19*, 563–573.

(40) Sellappan, R.; Nielsen, M. G.; González-Posada, F.; Vesborg, P. C. K.; Chorkendorff, I.; Chakarov, D. Effects of Plasmon Excitation on Photocatalytic Activity of Ag/Tio2 and Au/Tio2 Nanocomposites. *J. Catal.* **2013**, *307*, 214–221.

(41) Choudhury, B.; Bayan, S.; Choudhury, A.; Chakraborty, P. Narrowing of Band Gap and Effective Charge Carrier Separation in Oxygen Deficient Tio2 Nanotubes with Improved Visible Light Photocatalytic Activity. *J. Colloid Interface Sci.* **2016**, *465*, 1–10.

(42) Ge, M.-Z.; Cao, C.-Y.; Li, S.-H.; Tang, Y.-X.; Wang, L.-N.; Qi, N.; Huang, J.-Y.; Zhang, K.-Q.; Al-Deyab, S. S.; Lai, Y.-K. In Situ Plasmonic Ag Nanoparticle Anchored Tio2 Nanotube Arrays as Visible-Light-Driven Photocatalysts for Enhanced Water Splitting. *Nanoscale* **2016**, *8*, 5226–5234.

(43) Li, X.; Chen, G.; Yang, L.; Jin, Z.; Liu, J. Multifunctional Au-Coated Tio2 Nanotube Arrays as Recyclable Sers Substrates for Multifold Organic Pollutants Detection. *Adv. Funct. Mater.* **2010**, *20*, 2815–2824.

(44) Ansari, S. A.; Cho, M. H. Highly Visible Light Responsive, Narrow Band Gap Tio(2) Nanoparticles Modified by Elemental Red Phosphorus for Photocatalysis and Photoelectrochemical Applications. *Sci. Rep.* **2016**, *6*, 25405.

(45) Scherr, F. F.; Sarmah, A. K.; Di, H. J.; Cameron, K. C. Modeling Degradation and Metabolite Formation Kinetics of Estrone-3-Sulfate in Agricultural Soils. *Environ. Sci. Technol.* **2008**, *42*, 8388–8394.

(46) Zhou, W.; Liu, H.; Wang, J.; Liu, D.; Du, G.; Cui, J. Ag2o/Tio2 Nanobelts Heterostructure with Enhanced Ultraviolet and Visible Photocatalytic Activity. *ACS Appl. Mater. Interfaces* **2010**, *2*, 2385.

(47) Lin, Z.; Wang, X.; Liu, J.; Tian, Z.; Dai, L.; He, B.; Han, C.; Wu, Y.; Zeng, Z.; Hu, Z. On the Role of Localized Surface Plasmon Resonance in Uv-Vis Light Irradiated Au/Tio2 Photocatalysis Systems: Pros and Cons. *Nanoscale* **2015**, *7*, 4114–4123.

(48) Li, X.; Ye, J. Photocatalytic Degradation of Rhodamine B over Pb3nb4o13/Fumed Sio2 Composite under Visible Light Irradiation. *J. Phys. Chem. C* **2007**, *111*, 13109–13116.

(49) Sridharan, K.; Park, T. J. Thorn-Ball Shaped Tio2 Nanostructures: Influence of Sn2+ Doping on the Morphology and Enhanced Visible Light Photocatalytic Activity. *Appl. Catal., B* **2013**, *134–135*, 174–184.